

# Image-based Multi-scale Mechanical Analysis of Strain Amplification in Neurons Embedded in Collagen Gel

Victor W. L. Chan<sup>a</sup>, William R. Tobin<sup>a</sup>, Sijia Zhang<sup>b</sup>, Beth A. Winkelstein<sup>b</sup>, Victor H. Barocas<sup>c</sup>, Mark S. Shephard<sup>a</sup>, Catalin R. Picu<sup>a,d</sup>

<sup>a</sup>Scientific Computational Research Center, Rensselaer Polytechnic Institute, Low Center for Industrial Innovation, Troy, NY 12180;

<sup>b</sup>Department of Bioengineering, University of Pennsylvania, Philadelphia, PA 19104;

<sup>c</sup>Department of Biomedical Engineering, University of Minnesota, Minneapolis, MN 55455;

<sup>d</sup>Department of Mechanical, Aerospace and Nuclear Engineering, Rensselaer Polytechnic Institute, Troy, NY 12180

## ARTICLE HISTORY

Compiled January 28, 2018

## ABSTRACT

A general multi-scale strategy is presented for modeling the mechanical environment of a group of neurons that were embedded within a collagenous matrix. The results of the multi-scale simulation were used to estimate the local strains that arise in neurons when the extracellular matrix is deformed. The distribution of local strains was found to depend strongly on the configuration of the embedded neurons relative to the loading direction, reflecting the anisotropic mechanical behavior of the neurons. More importantly, the applied strain on the surrounding extracellular matrix was amplified in the neurons for all loading configurations that were considered. In the most severe case, the applied strain was amplified by at least a factor of 2 in 10% of the neuron by volume. The approach presented in this paper provides an extension to the capability of past methods by enabling the realistic representation of complex cell geometry into a multi-scale framework. The simulation results for the embedded neurons provide local strain information that is not accessible by current experimental techniques.

## 1. Introduction

In early studies of tissue mechanics (Fung 1993), the focus was on developing constitutive equations that described the mechanical behavior of a tissue as a continuous, homogeneous entity. Even the continuous tissue mechanics problem is extremely difficult, with issues such as viscoelasticity (Limbert and Middleton 2004; Peña et al. 2010), nonlinearity (Fung 1993), multiphasicity (Mow et al. 1980; Simon 1992), anisotropy (Fung 1993; Humphrey 2001; Ehret and Itskov 2009), active stress generation (Ambrosi and Pezzuto 2011), damage (Alastrué et al. 2007), and growth and remodeling (Humphrey and Rajagopal 2002; Menzel and Kuhl 2012) all coming into play under various circumstances. Much of the work in biomechanics has attempted to capture these different complexities at a continuum level given the macroscopic nature of humans and the apparent continuity of the tissue when viewed on the macroscopic scale.

---

Corresponding Author: Catalin R. Picu, Tel: +518 276-2195, E-mail: picuc@rpi.edu

More recently, however, it has been recognized that the essential unit that responds to a macroscopic load is in fact microscopic, such as a somatosensory nerve ending (Quindlen et al. 2016), a chondrocyte within articular cartilage (Guilak and Mow 2000), a cell remodeling its scaffold in an engineered blood vessel (Isenberg et al. 2006; Syedain et al. 2017), or - most relevant to the current work - a neurite undergoing physiological and excessive stretch in collagen constructs mimicking (spinal) ligaments (Sperry et al. 2017; Zhang et al. 2017a). In each of these cases, a macroscopic, tissue-scale loading condition is transferred to the microscopic, cell-scale stress, which in turn drives the cellular response. If we hope to understand the microscopic response to a macroscopic load, a scale-bridging strategy is needed.

The constrained-mixture approach (Humphrey and Rajagopal 2002) has been effective in predicting growth and remodeling at the continuum scale, but it does not account for the local cell stress that arises. As such, constrained-mixture models are not designed to address the effect of local strain field variations due to the presence of a cell, as observed experimentally in fibroblast-populated collagen gels (Pizzo 2005).

Inspired by classic work in the theory of composite materials (Hashin 1962), numerous studies have now been made where models are constructed of a cell surrounded by acellular material. In proposed cases, the approach employed is to place a cell of idealized shape (sphere or ellipsoid) in the center of the cubic domain made up of an acellular material. A notable extension is the multi-cell simulation study of Marquez, Genin, and Elson (Marquez et al. 2010), in which cylindrical or ellipsoidal cells were progressively added to the system, and an exponential increase in the tangent moduli of the extracellular matrix was observed when the cells percolated the domain. Another contribution (Lai et al. 2013) was the replacement of the closed-form constitutive equation with a multi-scale model that allows better representation of the extracellular matrix structure.

In spite of these recent advances, there is still more work to be done in pursuing a realistic representation of the cell's or tumor's mechanical environment under a given tissue load. Perhaps the most salient missing feature of current models is the fact that the microscopic entity is rarely spherical in shape. For example, cells spread and polarize within a collagen matrix, e.g., (Guido and Tranquillo 1993; Friedl et al. 1998), and a malignant tumor can have an extremely complex geometry (Cristini et al. 2003). There is a compelling need for methods that can account for the detailed microscale geometry when downscaling mechanical information.

Major barriers to a realistic representation of complex cell geometry include the generation of a model geometry from experimentally measured images and the subsequent mesh generation on that model geometry. Furthermore, the number of degrees of freedom required to represent properly the complex cell geometry is large, and when coupled with a multi-scale framework that is required to model the fibrous architecture of the extracellular matrix, the computational demand can become prohibitive. In this work, we addressed some of those challenges by developing a multi-scale model of a group of neurons embedded within a collagenous matrix. The objective in this work was to develop a general modeling strategy in which (1) confocal microscopy or another three-dimensional imaging modality is used to generate a realistic representation of a complex cell geometry, (2) that geometric model, along with the surrounding extracellular matrix, is converted to a finite-element mesh, (3) a multi-scale model is implemented on that mesh using a network microstructural model at each Gauss point (Chandran and Barocas 2007; Stylianopoulos and Barocas 2007), and (4) the solution of the mechanics problem is used to determine the distribution of strains within the cell.

Although the approach described herein is general, it is focused on the specific experimental system in which dorsal root ganglion (DRG) neurons are embedded in a collagen gel. This model system and others like it (Zhang et al. 2016, 2017a,b), allow detailed study of the cellular mechanisms of neuronal injury in a more controllable environment than can be achieved *in vivo*. As such, it has the potential to provide insight into the mechanism of neuronal injury under mechanical load, with markers of neuronal injury being quantified in response to different macroscopic strains and/or strain rates (Zhang et al. 2016). To summarize the experimental system, neurons were embedded in collagen gels to mimic the innervation of ligamentous tissue, such as that found in the spinal facet capsular ligament (McLain and Pickar 1998; Kallakuri 2012) and the knee joint capsule (Schultz et al. 1984; Khalsa et al. 1996). This *in vitro* system has been utilized to study the effects of macroscopic and microscopic scale tissue mechanics on neuronal responses in the context of pain. Previous studies using this and similar neuron-collagen culture models suggest that neuronal activation and pain signaling can be modulated by the macroscopic strain and collagen organization of the surrounding extracellular matrix (Zhang et al. 2016, 2017a). However, the system does not at present enable experimental evaluation of detailed neuronal mechanics, which is important for understanding the local mechanisms of neuronal mechanosensing and/or injury due to tissue loading. Therefore, an image-based multi-scale model that complements that neuron-collagen *in vitro* system is needed to investigate the relationships between macroscopic tissue deformations and mechanical changes in neurons.

The complex geometry of the neurons is incorporated into our model by employing tools (Simmetrix 2017) that are capable of generating geometric models from experimental images (Klaas et al. 2014, 2013) and of meshing the resulting geometric model (Shephard 2000). Additionally, the large computational demands of a multi-scale model on the resulting mesh are accommodated by the adaptive multi-scale simulation infrastructure (AMSI) library (Delalondre et al. 2010; Tobin et al. in preparation), which was designed to handle massively parallel simulations simultaneously on multiple scales. From this model, we observed strong strain amplification in the neurons due primarily to their complex geometry. The results provide a relation between the applied far field and the neuronal strain leading to the onset of pain.

## 2. Representation of Complex Cell Geometry

A realistic representation of complex cell geometry was generated from three-dimensional (3D) voxelated data that originated from a stack of image slices. In this work, confocal Z-stack images were taken from an unloaded 3D neuron-collagen culture system. Briefly, DRG were harvested from embryonic day 18 rats, dissociated and embedded in a collagen Type I gel (2mg/ml; Corning Inc; Corning, NY), using methods described in prior studies (Cullen et al. 2012; Zhang et al. 2016, 2017a). The structure of neurons was visualized by fluorescence labeling of the cytoskeletal protein  $\beta$ III-tubulin (Abcam Cambridge, MA), as described previously (Zhang et al. 2016, 2017a). A Zeiss LSM 510 confocal microscope (Carl Zeiss Inc; Thornwood, NY) was used to image the neurons. Z-stack images ( $2\mu\text{m}$  thick) were taken at a resolution of  $0.22\mu\text{m}/\text{pixel}$  with a 40X objective. Five consecutive images, each having a thickness of  $2\mu\text{m}$ , were used to reconstruct the neuronal structure in 3D. All images were segmented using *ImageJ* (Schneider et al. 2012) based on the positive labeling of  $\beta$ III-tubulin for model construction, and speckle noise in the background was removed in Adobe Photoshop (Adobe Systems Incorporated; San Jose, CA). Sample raw confocal

Z-stack images that were used in our model are shown in Fig. 1.

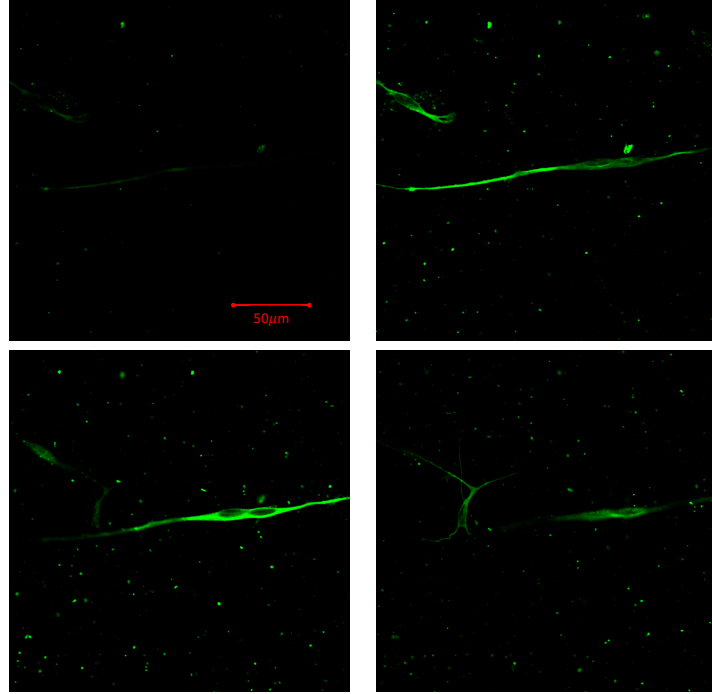


**Figure 1.** Sample of raw images taken from Zeiss LSM 510 confocal microscope that were used in our model. The scale bar in the top left image represents  $50 \mu\text{m}$  and applies to all images. The images were stacked from top to bottom in the following order: top left, top right, bottom left, and bottom right.

The confocal images were converted to a 3D voxelated data set using *ImageJ* (Schneider et al. 2012). Noise in the voxelated data due to the limited level of contrast in the imaging technique is removed using a combination of erosion/dilation, manual reassignment, small object removal, and smoothing operations via the *ImageToModel* tool (Klaas et al. 2013, 2014; Simmetrix 2017). Once processed, the voxelated data are converted into a discrete geometry via an initial triangulation that is based on voxel level operations where mesh coarsening is not performed until after the surface triangulation has been smoothed (Klaas et al. 2013). Quantization artifacts on the surface of the geometry due to the voxel nature of the data are removed using a smoothing algorithm that consists of three steps (Klaas et al. 2013): (1) calculate the surface normal of the desired surface geometry at each mesh face based on the normals of neighboring mesh faces; (2) smooth surface normals on the mesh to obtain the normals of desired surface geometry; (3) adjust the mesh vertex positions iteratively to create a surface that matches the smoothed surface normals.

Subsequently, the discrete geometry generated from the voxelated neuron-in-gel data was enclosed in a box that represents the domain of the collagen gel. The neuron-gel interface was treated as perfectly bonded. A graded mesh of 82,105 tetrahedral elements was generated on the non-manifold neuron-in-gel geometry using the SimModele tool of Simmetrix Inc. (Shephard 2000; Simmetrix 2017). The neuron-in-gel voxelated data, discrete geometry, and corresponding mesh are shown in Fig. 2.

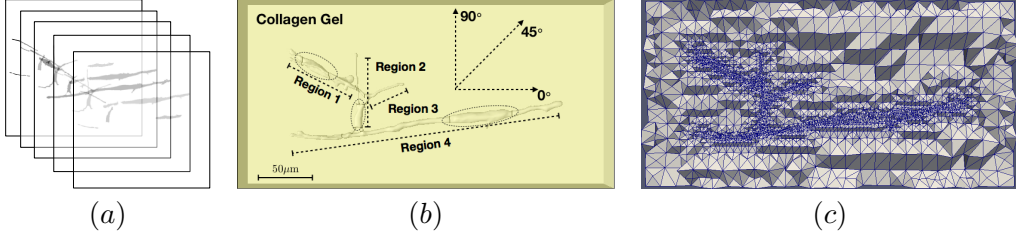


**Figure 2.** (a) Stack of confocal images of neurons from Fig. 1. (b) Geometric model of neurons that are embedded in a collagen gel. The region enclosing the neurons is the collagen gel. (c) Cut in neuron-in-gel model showing the generated mesh. In (b), the neuron cell bodies are marked with dashed ovals. The axes of load directions corresponding to 0°, 45°, and 90° and regions of neuron corresponding to different local axes are also schematically illustrated.

### 3. Multi-Scale Method for Modeling Collagen Gel

Collagen gels have been modeled in the past using a multi-scale formulation based on volume averaging of fiber-network representative volume elements (RVEs) (Chandran and Barocas 2007; Stylianopoulos and Barocas 2007; Lai et al. 2012; Lake et al. 2012). Such a multi-scale formulation is also employed in this study to model the collagen gel surrounding the neurons. The multi-scale formulation consists of two scales: the collagen-network scale on which the network of collagen fibrils is represented explicitly, and the macroscopic scale that represents the continuum tissue level. Quantities corresponding to the collagen-network (or microscopic) and macroscopic scales are denoted with  $(m)$  and  $(M)$  superscripts, respectively.

The collagen-network scale is represented by a fiber network, which defines the RVE. Each RVE is generated from the Delaunay triangulation of randomly placed seed points - the edges of the triangulation represent the fibers of the network. Each fiber only carries an axial load, with the axial forces in tension and compression given by

$$T^{(m)} = \begin{cases} H_C \lambda_f + h_C & \text{if } \lambda_f < \lambda_C \\ \frac{E_f A_f}{B} \left[ \exp\left(0.5B(\lambda_f^2 - 1)\right) - 1 \right] & \text{if } \lambda_f \in [\lambda_C, \lambda_S] \\ H_S \lambda_f + h_S & \text{if } \lambda_f > \lambda_S \end{cases} \quad (1)$$

where

$E_f$  : linear modulus of a collagen fiber.

$A_f$  : cross-sectional area of fiber.

$B$  : constant parameter that controls nonlinearity.

$\lambda_f \equiv \frac{l}{l_0}$  where  $l$  and  $l_0$  are the current and initial lengths, respectively, of the fiber.

$\lambda_S$  : fiber stretch value at which the fiber relation transitions from nonlinear to linear.

$\lambda_C$  : fiber compression value at which the fiber relationship transitions from nonlinear to linear.

$H_n \equiv E_f A_f \lambda_n \exp(0.5B(\lambda_n^2 - 1))$  for  $n = S$  or  $C$ .

$h_n \equiv \frac{E_f A_f}{B} \left[ \exp(0.5B(\lambda_n^2 - 1)) - 1 \right] - H_n \lambda_n$  for  $n = S$  or  $C$ .

The fiber force vs. stretch in tension transitions from a nonlinear to linear relationship when the fiber is stretched beyond  $\lambda_S$ , while the fiber force in compression transitions from a nonlinear to linear relationship when the fiber is compressed below  $\lambda_C$ . The transition to a linear fiber force relationship for large fiber stretch in tension is consistent with experimental measurements of single collagen fibers (Eppell et al. 2006; Svensson et al. 2010).

Displacement boundary conditions are imposed in order to solve for network equilibrium in the RVE. The displacements at the corners of the RVE are dictated by the deformation state of the macroscopic scale via

$$u_i^{(c,m)} = (F_{ij}^{(M)} - \delta_{ij}) \frac{x_j^{(c,m)}}{L^{(m)}}, \quad (2)$$

where  $F_{ij}^{(M)}$  is the deformation gradient tensor of the macroscopic scale,  $u^{(c,m)}$  are the displacements at the corners of the RVE, and  $x_j^{(c,m)}/L^{(m)}$  are the coordinates of the corners of the RVE. In Eq. (2),  $x_j^{(c,m)}$  are coordinates of a dimensionless computational domain that is a cube spanning the domain defined by (-0.5,0.5) in each of the coordinate axes. The scale conversion,  $1/L^{(m)}$ , relates the unit lengths between the computational and physical domains. The scaling parameter,  $L^{(m)}$ , is determined by comparing the average fiber length in the RVEs to the average fiber length in the collagen gel of density 2 mg/mL used in (Zhang et al. 2016). The mean fiber length in such a network is 1.81  $\mu\text{m}$  (Lindström et al. 2013), while the mean segment length in the RVEs used in this work is 0.26. Based on these values  $L^{(m)} = 7 \mu\text{m}$ .

Equation (2) is valid because the center of the RVE is defined at the origin of the computational domain. We control the motion of all nodes on the surface of the RVE and allow the interior degrees of freedom to relax such to minimize the RVE potential energy. The displacements on each node lying on the surface of the RVE are determined via linear interpolation of  $x_j^{(c,m)}$ .

Upon solving for network equilibrium in each RVE, the volume-averaged Cauchy stress tensor of the collagen-network scale is computed from the forces acting on nodes that lie on the surface of the RVE (boundary cross-links) (Chandran and Barocas 2007)

$$s_{ij}^{(m)} = \frac{1}{V^{(m)}} \sum_{\text{boundary cross-links}} x_i^{(m)} T_j^{(m)}, \quad (3)$$

where  $V^{(m)}$  is the current volume of the RVE,  $T_j^{(m)}$  is the  $j^{\text{th}}$  component of the fiber force, and  $s_{ij}^{(m)}$  are elements of the microscopic stress tensor. The macroscopic volume-averaged Cauchy stress tensor is determined from scaling  $s_{ij}^{(m)}$  by  $L^{(m)}$ :

$$\sigma_{ij}^{(M)} = s_{ij}^{(m)} \left( \frac{1}{L^{(m)}} \right)^2. \quad (4)$$

This scaling is needed due to the difference in length scales between the physical macroscopic domain and the non dimensional microscopic computational domain. The averaged Cauchy stress tensor of Eq. (4) is used to solve the volume-averaged macroscopic

force balance (Chandran and Barocas 2007)

$$\sigma_{ij,i}^{(M)} = \frac{1}{V^{(m)}} \int_{\partial V^{(m)}} \left( s_{ij}^{(m)} - \sigma_{ij}^{(M)} \right) u_{k,i}^{(m)} n_k dA^{(m)}, \quad (5)$$

where  $u_k^{(m)}$  is the displacement of the RVE boundary on the microscale and  $n_k$  is the unit normal vector of the corresponding surface. Equation (5) arises from integration of the microscopic-scale (RVE) Cauchy stress balance,  $\sigma_{ij,i}^{(m)} = 0$ . If the RVE did not deform, then the averaged equation would just be  $\sigma_{ij,i}^{(M)} = 0$ . When the RVE deforms, however, and that deformation is position-dependent, then the average of the divergence of the stress ( $\sigma_{ij,i}^{(m)}$ ) is no longer equal to the divergence of the average stress ( $\sigma_{ij,i}^{(M)}$ ), and a correction term must be introduced, analogous to the corresponding term in the Reynolds transport theorem (Whitaker 1999). This term is expressed by the right-hand side of Eq. (5) and accounts for the correlation between RVE stress and boundary displacement.

#### 4. Constitutive Relationship for Modeling of Neurons

Cross-linked axially-aligned microtubule bundles are a major structural feature of axons and give rise to macroscopic mechanical anisotropy (Peter and Mofrad 2012). To account for such mechanical anisotropy, the axons are modeled as a transversely isotropic hyperelastic material (Bonet and Burton 1998; Bonet and Wood 2008). The elements of the Cauchy stress tensor and spatial (Eulerian) elasticity tensor are expressed in terms of neo-Hookean (nh) and transversely isotropic (trns) components (Bonet and Burton 1998)

$$\sigma_{ij} = \sigma_{ij}^{\text{nh}} + \sigma_{ij}^{\text{trns}} \quad \text{and} \quad c_{ijkl} = c_{ijkl}^{\text{nh}} + c_{ijkl}^{\text{trns}}, \quad (6)$$

respectively, where

$$\begin{aligned} \sigma_{ij}^{\text{nh}} &= \frac{\mu}{J} (b_{ij} - \delta_{ij}) + \lambda(J-1)\delta_{ij} \\ \sigma_{ij}^{\text{trns}} &= \frac{2\beta}{J} (a_r a_r - 1) \delta_{ij} + \frac{2}{J} [\alpha + 2\beta \ln J + 2\gamma(a_r a_r - 1)] a_i a_j - \frac{\alpha}{J} (b_{is} a_s a_j + a_i b_{jr} a_r) \\ c_{ijkl}^{\text{nh}} &= \lambda(2J-1) \delta_{ij} \delta_{kl} + \frac{2}{J} [\mu - \lambda J(2J-1)] \delta_{ik} \delta_{jl} \\ c_{ijkl}^{\text{trns}} &= \frac{8\gamma}{J} a_i a_j a_k a_l + \frac{4\beta}{J} (a_i a_j \delta_{kl} + \delta_{ij} a_k a_l) - \frac{\alpha}{J} (a_i a_l b_{jk} + b_{ik} a_j a_l) - \frac{4\beta}{J} (a_r a_r - 1) \delta_{ik} \delta_{jl}. \end{aligned} \quad (7)$$

In Eq. (7),  $b_{ij}$  are elements of the left Cauchy-Green strain tensor and  $a_i$  is a component of the mapping of the direction of anisotropy in the undeformed state,  $A_k$ , to the current state via the deformation gradient,  $F_{ik}$ , via  $a_i \equiv F_{ik} A_k$ .  $\lambda$  and  $\mu$  are the Lamé constants that define the material properties of the isotropic component, while  $\beta$ ,  $\gamma$ , and  $\alpha$  are parameters that define the material properties of the anisotropic component.

The parameters of Eq. (7) can be written in terms of material constants as

$$\begin{aligned}\lambda &= \frac{2\mu(\nu + n\nu^2)}{m} & \gamma &= \frac{E_A(1 - \nu)}{8m} - \frac{\lambda + 2\mu}{8} + \frac{\alpha}{2} - \beta \\ \alpha &= \mu - G_A & m &= 1 - \nu - 2n\nu^2 \\ \beta &= \frac{\mu\nu^2(1 - n)}{2m} & n &= \frac{E_A}{2\mu(1 + \nu)},\end{aligned}\quad (8)$$

where  $\mu$  is the shear modulus,  $G_A$  is the axial shear modulus,  $\nu$  is the Poisson ratio, and  $E_A$  is axial Young's modulus. In our analysis, the shear modulus is set to be isotropic such that  $G_A = \mu$  and  $\alpha = 0$ . All the constants in Eq. (8) are set once all material constants ( $\mu$ ,  $G_A$ ,  $\nu$ , and  $E_A$ ) are specified.

## 5. Parameter Specifications

### 5.1. Parameters of Collagen Network

Collagen I gels identical to those in which the neurons were embedded were subjected to uniaxial tensile loading at 0.5mm/s up to 25% strain using an Instron 5865 (Instron, Norwood, MA), as described in Zhang et al. (2016). The measured stress-strain curve is shown in Fig. 3(a). This data is used to calibrate three parameters ( $E_f$ ,  $B$ , and  $\lambda_S$ ) of the constitutive behavior of fibers of the collagen network. The prediction of the model gel is obtained with an RVE containing a network of density identical to that of the physical gel. Table 1 shows the set of parameters used for the collagen network.

Parameter	Specification	Source
$E_f$	200 kPa	Fit to experimental data.
$A_f$	$0.0825 \mu\text{m}^2$	Based on Dutov et al. (2016)
$B$	20	Fit to experimental data.
$\lambda_S$	1.13	Fit to experimental data.
$\lambda_C$	1.0	Chosen by authors.
$H_S$	$297.25 \mu\text{N}$	Calculated from $E_f$ , $A_f$ , $B$ , and $\lambda_S$ .
$H_C$	$16.5 \mu\text{N}$	Calculated from $E_f$ , $A_f$ , $B$ , and $\lambda_C$ .
$h_S$	$-322.74 \mu\text{N}$	Calculated from $E_f$ , $A_f$ , $B$ , $\lambda_S$ , and $H_S$ .
$h_C$	$-15.67 \mu\text{N}$	Calculated from $E_f$ , $A_f$ , $B$ , $\lambda_C$ , and $H_C$ .
$L^{(m)}$	7 $\mu\text{m}$	Based on mean segment length of RVE reported in Section 3.

**Table 1.** Parameters of the constitutive behavior of the fiber network used to model the collagen gel.

As seen in Fig. 3(a), a good fit to the experimental stress-strain curve was obtained using the parameters listed in Table 1. The value of  $A_f$  was chosen according to (Dutov et al. 2016) where the fiber radius of rat tail collagen I was measured to be 162 nm. The parameters  $E_f$  and  $B$  were adjusted to capture the stiffening in the stress-strain curve at approximately 11% strain observed experimentally, while  $\lambda_S$  was adjusted to capture the stiffness of the linear regime in the stress-strain curve at large strains. Since the fibers in this model only have axial forces, the value of  $\lambda_C$  was selected to give a stiffness in compression that is significantly smaller than that in tension. This represents the softening associated with buckling or off-axis loading of fibers in

compression. By choosing  $\lambda_C = 1.0$ , the response in compression remains linear for all strains encountered in simulations. The fiber-force vs. strain curve for the parameters listed in Table 1 is plotted in Fig. 3(b).

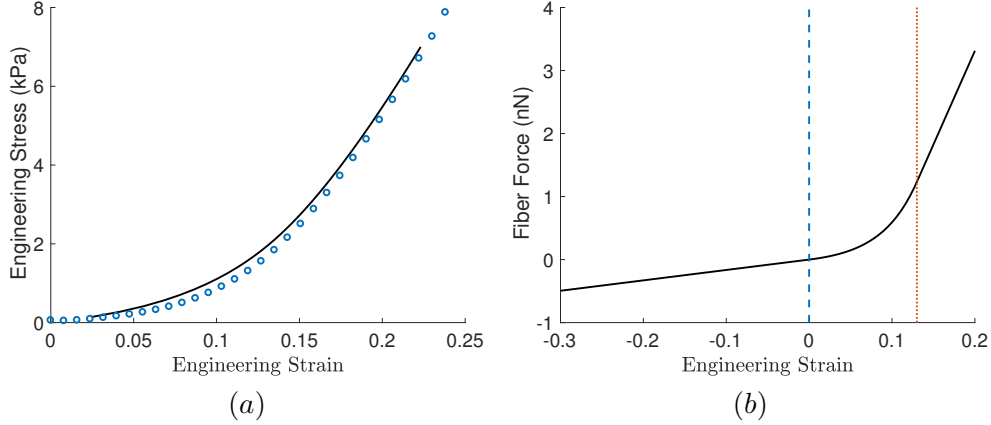


**Figure 3.** Plots of (a) model network and experimental gel stress-strain, and (b) model collagen fiber force vs. fiber-strain curve for parameters listed in Table 1. In (a), the result from simulation is plotted using black solid line, while experimentally measured data is plotted with blue dots. The line connecting the blue dots was added to aid visual interpretation. In (b), the values of  $\lambda_C$  and  $\lambda_S$  are marked as blue dashed and red dotted vertical lines, respectively.

For the parameters in Table 1, fiber alignment was also examined. Although fibers in our simulations rearrange in 3D, a two-dimensional (2D) orientation index,  $P_2$ , is considered in order to make the connection with experimental observations. The value of  $P_2$  is calculated from the angle  $\theta$  between the projection of the fiber in the plane of analysis and the direction of stretch and is given by

$$P_2 = 2 < \cos^2 \theta > - 1, \quad (9)$$

where  $< x >$  denotes the ensemble average of  $x$  over all fibers. The value of  $P_2$  ranges from 1 in which the fibers are completely aligned in the stretch direction to -1 in which all fibers are orthogonal to the stretch direction. When  $P_2 = 0$ , the fiber network is randomly oriented.

Experimentally, the fiber alignment in innervated collagenous tissue was measured using quantitative polarized light imaging (QPLI) (Quinn and Winkelstein 2008, 2009) where alignment angle  $\alpha$  and retardation  $\delta$  were measured in each pixel. The customized QPLI system used in these experiments (Zhang et al. 2016) is comprised of a fiber-optic light source (Dolan-Jenner Industries Inc., Boxborough, MA), a motor-controlled linear polarizer (Edmund Optics, Barrington, NJ) that rotates at 750 rpm, and a circular analyzer mounted to a high-speed camera (Phantom-v9.1; Vision Research Inc, Wayne, NJ) (Zhang et al. 2016). The QPLI system was integrated with a mechanical testing device, and collagen I gels were placed between the rotating polarizer and the circular analyzer. Polarized light images were acquired during tensile loading at 500 fps with 14.5 pixel/mm resolution and processed using harmonic analysis to extract the alignment angle and retardation (Tower et al. 2002; Quinn and Winkelstein 2008). The orientation index  $P_2$  is calculated from  $\alpha$  and  $\delta$  of the QPLI

method via (see Appendix A)

$$P_2 = 2 \int_0^\pi p(\theta) \cos^2 \theta d\theta - 1$$

$$p(\theta) = \frac{1}{N} \sum_{i=1}^N \left[ \frac{C - 2\delta_i}{\pi C} + \frac{4\delta_i}{\pi C} \cos^2(\theta - \alpha_i) \right], \quad (10)$$

where the probability distribution,  $p(\theta)$ , is a convenient approximation of the actual distribution of collagen orientation in the sample. In Eq. (10),  $\delta_i$  and  $\alpha_i$  are the retardation and alignment angle, respectively, of the  $i^{th}$  pixel. The proportionality constant  $C$  relates  $\delta_i$  to the difference in the eigenvalues of the orientation tensor. A method to infer  $C$  based on the experimental conditions was not available. Hence, we fit  $C$  to the experimental  $P_2$  vs. strain curve. When  $C = 0.5$ , good agreement between the experimental and simulated fiber orientation was achieved (Fig. 4). Such agreement between simulation and experimental results reinforces our choice of the RVE fiber network parameters listed in Table 1.

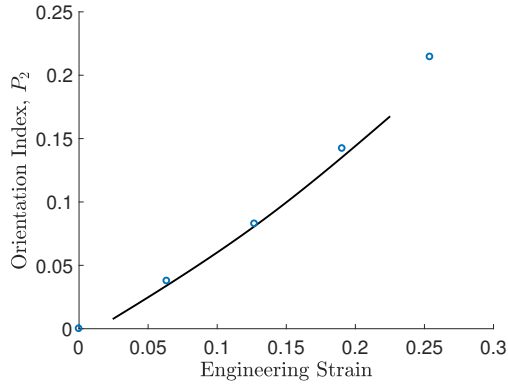


**Figure 4.** Fiber alignment metric  $P_2$  of simulation using parameters listed in Table 1 and of experimental results using  $C = 0.5$  for Eq. (10). Results from simulation plotted using black solid line, while experimentally measured data are plotted in blue dots.

### 5.2. Parameters of the Constitutive Description of the Neurons

The value of  $E_A$  in Eq. (8) is based on the study by Peter and Mofrad (Peter and Mofrad 2012), where the mechanical behavior of axonal microtubule bundles under tension was simulated with a discrete bead-spring model. To apply their results for microtubule bundles to our neuron model, we assume that only the microtubule bundles carry force in the axon and that the stress of the microtubule bundles can be redistributed over the cross-sectional area of the axon. Since the microtubules are the stiffer component of the cytoskeleton (Fletcher and Mullins 2010), the mechanical contribution from the actin filaments (membrane cortex) is ignored. Based on these assumptions, the axial stiffness of the axon can be related to the axial stiffness of the microtubule bundles,  $E_{MTb}$ , by

$$E_A = \frac{E_{MTb} A_{MTb}}{A_A}, \quad (11)$$

where  $A_{MTb}$  and  $A_A$  are the cross-sectional areas of the microtubule bundle and axon, respectively. Peter and Mofrad (Peter and Mofrad 2012) suggested that the stress-strain relationship of the microtubule bundle is well represented by a power-law fit that results in a strain-dependent elastic modulus. For this study,  $E_{MTb}$  was taken to be  $1 \times 10^5$  kPa, which corresponds to a low strain of less than 0.1%. The value of  $A_{MTb}$  was determined to be  $0.00933 \mu\text{m}^2$  based on the diameter of each microtubule and the number of microtubule cross sections within a microtubule bundle, see Ref. (Peter and Mofrad 2012) for schematic. We assume that the cross-section of the microtubule bundle contains 19 rows of microtubules, each with a diameter of 25 nm. Lastly, the value of  $A_A$  was determined to be  $13.3 \mu\text{m}^2$ , based on an average axon diameter of approximately 4  $\mu\text{m}$  in the neuron.  $E_A$  is determined from Eq. (11) to be 70 kPa.

The parameters used in Eq. (8) for modeling the neuron structure are listed in Table 2. The transverse stiffness of the axons and cell bodies was set to 1.5 kPa based on

Parameter	Specification	Source
$E_A$	70 kPa	Calculated from Eq. (11).
$E_T$	1.5 kPa	Based on Simon et al. (2016)
$\nu$	0.3	Chosen by authors.
$\mu$	0.577 kPa	Calculated from $E_T$ and $\nu$ .
$G_A (= \mu)$	0.577 kPa	Shear modulus assumed to be isotropic.
$t$	30 $\mu\text{m}$	From analysis in Section 7.
$n$	46.7	Calculated from $E_A$ , $\mu$ , and $\nu$ .
$m$	-7.7	Calculated from $\nu$ and $n$ .
$\lambda$	-0.67 kPa	Calculated from $\nu$ , $\mu$ , $n$ , and $m$ .
$\alpha$	0 kPa	Calculated from $\mu$ and $G_A$ .
$\beta$	0.154 kPa	Calculated from $\mu$ , $\nu$ , $n$ , and $m$ .
$\gamma$	-1.01 kPa	Calculated from $E_A$ , $\nu$ , $m$ , $\lambda$ , $\mu$ , and $\beta$ .

**Table 2.** Parameters for constitutive model of neuron.

the measurements of Simon et al. (Simon et al. 2016). The six constants in Eq. (8) are all determined when the values listed in Table 2 are fully specified.

The axial stiffness of the cell body was chosen based on the relative alignment of the microtubules. The microtubules transition from an almost perfectly aligned state in the axon to a generally unaligned state within the cell body (Mofrad and Kamm 2006). Within the cell body, the microtubules become progressively less aligned with the center of the cell body having the least alignment. Consequently, the axial stiffness within the cell body decreases and is lowest at the center. The cell bodies are modeled as a transversely isotropic hyperelastic material of axial stiffness represented by a function of position within a cell, Eq. 12.

$$E_A^{cell} = \left(1 - \frac{D}{t}\right) E_A. \quad (12)$$

In Eq. (12)  $D$  is the distance from an interior point of the cell body to the closest axon, and  $t$  is a constant describing the rate of change of  $E_A^{cell}$ . The geometry shown in Fig. 2(b) indicates that the parameter  $D$  ranges from 9 to 25  $\mu\text{m}$ . We select a value of  $t = 30 \mu\text{m}$  for our calculations. The axial stiffness of the neuron structure evaluated based on these parameters is shown in Fig. 5. The transition in the axial stiffness within the cell bodies presented in Eq. (12) is artificial. To understand how

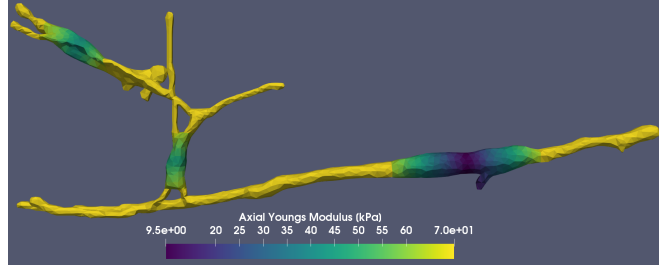


**Figure 5.** Axial stiffness of neuron structure analyzed.

this transition affects the final strain distribution in the neuron, the transition rate was varied by adjusting  $t$  in Eq. (12). Values of  $t = 28 \mu\text{m}$ ,  $30 \mu\text{m}$ , and  $50 \mu\text{m}$  were considered (discussed in Appendix B), and the strain distribution within the neurons was found to be insensitive to the parameter  $t$ .

## 6. Implementation

### 6.1. Adaptive multi-scale simulation infrastructure

Our multi-scale model is implemented using the adaptive multi-scale simulation infrastructure (AMSI) (Tobin et al. in preparation), which is designed to support massively parallel simulations on multiple scales. AMSI accommodates the computational demands of the multi-scale simulation by combining existing single-scale analysis codes into multi-scale analyses. The macroscopic simulation code and the microscopic simulation codes are independent codes coupled through the AMSI libraries. AMSI manages the parallel execution space for each code, as well as the parallel communication responsible for the transmission of required data between them.

The macroscopic-scale domain is discretized using an unstructured mesh that is partitioned across the parallel execution space of the scale. Figure 6 depicts the relationship between the two scales with respect to the macroscopic-scale unstructured mesh, an individual numerical integration point on that mesh, and the RVE-level microscopic-scale simulation corresponding to that macroscopic-scale location.

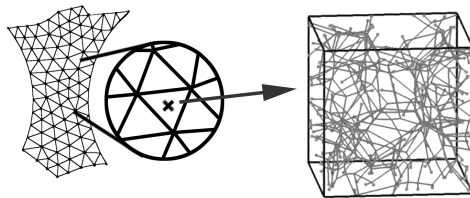


**Figure 6.** Schematic showing the hierarchy of scales in the multi-scale simulation

AMSI manages the relationship between the domains of the macroscopic and microscopic scale problem. At each macroscopic-scale numerical integration point, the deformation gradient  $F_{ij}$  is calculated and provided to the AMSI coupling system,

which uses a communication plan to provide the value to the collagen-network scale RVE simulation related to the integration point. This  $F_{ij}$  value is used by the collagen-network scale, as shown in Eq. (2), to establish the boundary conditions for the current state of the RVE problem. Once a solution has been reached for the collagen-network scale simulation, the macroscopic-scale volume-averaged Cauchy stress term  $\sigma_{ij}^{(M)}$  from Eq. (4) and stress derivative terms  $\sigma_{ij,k}^{(M)}$  are supplied to AMSI. These terms are communicated to the macroscopic scale and associated with the coupled integration point for use in assembling the macroscopic-scale linear algebraic system for the current Newton iteration.

Up- and down-scaling transformations of the coupling data currently occur in the user code after (or before) employing the communication plan. The down-scaling of the deformation gradient terms to generate the displacement on the corner of an RVE in equation 2 takes place at the collagen-network scale after the coupling communication. The up-scaling in equation 4 also takes place at the collagen-network scale, prior to communicating the stress terms to the macroscopic scale.

### **6.2. Computational Model Solved**

The solution to the macroscopic boundary value problem in Eq. (5) is obtained using the Finite Element-method (FEM). The domain of the embedded neuron is discretized by a mesh consisting of 82,105 linear tetrahedral elements - 14,250 in the neuron and 67,855 in the collagen gel - giving rise to more than 985k degrees of freedom (DOF) in the macroscopic scale.

The computation demands are substantially greater for the collagen-network scale where each fiber network RVE consists of, on average, 284 fiber cross links. Three DOF exist for each fiber cross link, giving rise to 852 DOF per RVE. Since there is a single RVE for each numerical integration point of the macroscopic mesh of the collagen gel, the total DOF for the collagen-network scale is more than 57 million (852 DOF/RVE  $\times$  67,855 RVEs).

The large computational demands of the neuron-in-gel multi-scale model requires both the macroscopic and microscopic scale calculations to be performed in parallel. We employ the AMSI libraries to manage the parallel execution space for each scale. For our simulations, a total of 2048 cores were used on the AMOS BlueGene/Q maintained by the Center for Computational Innovations at RPI. Each node on the AMOS system has a 16-core 1.6GHz A2 processor with 16GB of DDR3 RAM, thus 128 nodes were allocated to the execution of this problem, with 128GB of memory. Of the assigned cores, 128 were devoted to the macroscale computation, while the remaining 1920 cores were used to compute the microscale RVE simulations.

As the macroscale and microscale codes are assigned separate partitions of the parallel execution space, the simulation never sees 100% parallel utilization due to the need of each scale to block while waiting for the other to compute. In order to achieve good performance given this constraint, we consider the computational demand of each scale and partition the simulation scales to prioritize process utilization and reduce process idle time.

The DOF count at each scale provides an initial estimate of the computational demand of the problem, however the complexity of the physics and software implementation of each scale also contributes a heuristic weight which, when applied to the DOF count, allows a more appropriate comparison of the computational demand at each scale. Particularly, this approach justifies the use of a core ratio between the

macroscale and microscale problems other than one derived simply from the DOF count, which would be approximately 1:57 macroscale cores to microscale cores if only taking DOFs into account. Instead the ratio of 1:15 was heuristically determined to provide a better overall process utilization by minimizing core idle time.

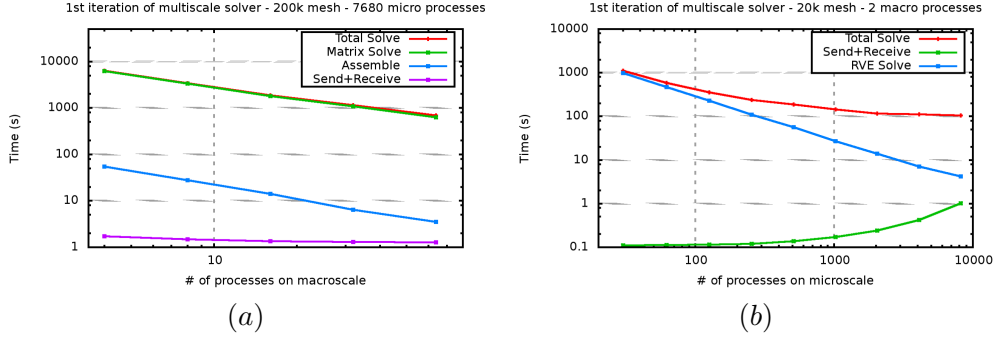


**Figure 7.** Strong-scaling the (a) macroscale and (b) microscale parallel allocations while holding the other scale allocation constant. Measurements taken with the multi-scale code applied to a different problem.

As the allocation and processing of individual microscale simulations is embarrassingly parallel, the allocation ratio can be scaled in favor of the microscale to reduce overall time-to-solution (see figure 7b). This approach sacrifices misroscale process utilization when holding the macroscale allocation and problem size constant as it increases the microscale idle time linearly since the time-to-solution of the macroscale is held constant. Increasing the allocation ratio in favor of the macroscale has less impact on the overall process utilization (see figure 7a) or time-to-solution as both of these are dominated by the work to be conducted at the microscale.

Increasing the total parallel allocation while holding the problem size and allocation ratio constant reduces time-to-solution while retaining the same process utilization characteristics up to the point where the microscale code begins to lose efficiency due to increasing communication overhead on a problem of constant size.

## 7. Results and Discussion

The embedded neuron model described above provides local strain information within the neuron structure that is inaccessible by current experimental procedures. Therefore, the neuron model serves as a computational microscope that can be used to probe the neuron's response to its mechanical environment under load. For this study, the collagen gel surrounding the neuron was subjected to grip strains of up to 16%, which corresponds to the threshold loading beyond which pain is reported to arise (Lee et al. 2004; Dong et al. 2012; Zhang et al. 2016; Ita et al. 2017; Zhang et al. 2017a).

The strain within the neuron was quantified by a complementary cumulative distribution function (ccdf) defined as

$$\text{ccdf}(X) = \int_X^{\infty} p_{\epsilon^*}(X) d\epsilon^* = \Pr[\epsilon^* \geq X], \quad (13)$$

where  $p_{\epsilon^*}(X)$  is the probability density function of  $\epsilon^*$ , and  $\epsilon^*$  is either the axial,  $\epsilon_{\text{ax}}$ , or transverse,  $\epsilon_{\text{trns}}$ , strain with respect to the local axon axis; the four regions corresponding to the different local axes in the neuron were shown schematically in

Fig. 2(b). Equation 13 is the probability that an arbitrary point within the neuron experiences an axial or transverse strain of *greater than or equal to*  $X$ . The value measured in Eq. (13) is approximately equal to the volume fraction of the neuron that experiences a strain of greater than or equal to  $X$ . In the analysis below, the Green-Lagrange strain was used for measuring deformation.

### ***7.1. Strain Distribution within Neuronal Bodies***

In vivo, a patch of tissue can be loaded in various ways depending on the activity or event imposing the load. To gain an understanding of the strain in the neuronal bodies under arbitrary loading, we examined the axial and transverse strain distributions in the neuron for the three different loading conditions shown in Fig. 2(b) for  $t = 30 \mu\text{m}$ . The model is rotated relative to the far-field loading direction in-plane because the structure considered is approximately planar. Color maps of the maximum principal strain in the neuron for a grip strain of 16% (painful ligament loading) and for  $0^\circ$ ,  $45^\circ$ , and  $90^\circ$  loading are plotted in Fig. 8. For all angles of loading, large portions of the neuron experience strains that are greater than the 16% applied grip strain. This result indicates that the applied strains on the collagen gel are amplified in the neuron, which could lead to neuronal damage even when the surrounding tissue is moderately loaded.

To gain a more quantitative understanding of the strain distribution in the neuron, we focused on the normal strains along and transverse to the axon axis, and computed their ccdf for two levels of far field strain (10% and 16% corresponding to non-painful and painful ligament loading, respectively) and three loading directions (Fig. 2(b)). The resulting ccdf are shown in Fig. 9. The shapes of the strain distributions vary significantly for different applied strains and loading directions. The strong dependence of the strain distribution on loading configuration reflects the anisotropic nature of the embedded neuron, where the axial stiffness is more than one order of magnitude greater than the transverse stiffness. Relative to the stiffness of the surrounding collagen gel, the axial stiffness of the neuron is larger while the transverse stiffness of the neuron is smaller.

In all cases, the strain magnitude within the neuron is larger for an applied strain of 16%, as expected; the black solid curve lies to the right (left) of the blue dashed curve for positive (negative) values of strain. Interestingly, aside from the axial strain case for  $0^\circ$  loading, the same fraction of the neuron volume experiences a strain that is greater than or equal to the applied grip strain, regardless of the strain magnitude or the loading direction; that is, the red dashed and solid lines intersect the same value on the ordinate of the ccdf. In the case of axial strain for  $0^\circ$  loading, the fraction of the neuron volume that amplifies the applied strain increases with grip strain.

The fraction of the neuron volume that experiences a value of strain that is greater than or equal to the far-field applied strain is listed in Table 3 for all cases plotted in Fig. 9. As seen in Table 3, the applied strain on the collagen gel is amplified in the neuron predominantly along the axial direction for  $0^\circ$  loading and in the transverse direction for  $45^\circ$  and  $90^\circ$  loading. For  $45^\circ$  loading, less than 0.1% of the neuron volume experiences an axial strain that is greater than or equal to the applied strain.

The values listed in Table 3 are consistent with how the embedded neuron is oriented relative to the different loading directions. When loading at  $0^\circ$  a majority of the neuron volume (regions 1, 2, and 4 in Fig. 2(b)) is loaded predominantly in the axial direction causing a larger fraction of the neuron to be amplified in the axial direction. On the

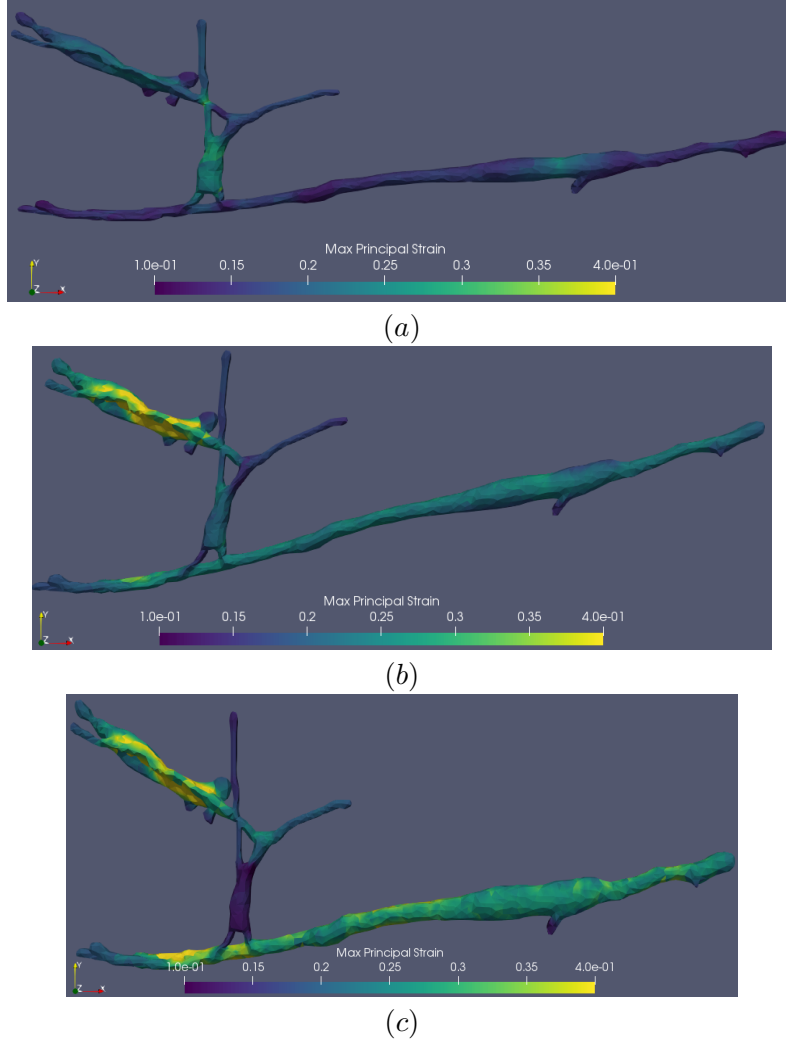


**Figure 8.** Color maps of maximum principal strain in neuron for grip strain of 16% for loading angles of (a)  $0^\circ$ , (b)  $45^\circ$ , and (c)  $90^\circ$ . The color bar ranges from 10% to 40% maximum principal strain.

other hand, when loading at  $90^\circ$  a majority of the neuron volume (regions 1, 3, and 4 in Fig. 2(b)) are loaded predominantly in the transverse direction causing a larger fraction of the neuron to be amplified in the transverse direction. The amplification of the applied strain in the transverse direction is significantly greater because the neuron is much more compliant in the transverse direction relative to the axial direction. The neuron also experiences a significant strain amplification in the transverse direction when loaded at  $45^\circ$  because the axial direction of region 1 lies perpendicular to the  $45^\circ$  loading direction.

Physiologically more important are the tails of the strain distributions, which represent the largest strains experienced by the neuron. The minimum strains experienced by the most-deformed 10% of the neuron (by volume fraction) are listed in Table 4 for each loading case. Consistent with above, the largest minimum strain experienced by the most-deformed 10% of the neuron occurs in the axial direction for  $0^\circ$  loading and in the transverse direction for  $45^\circ$  and  $90^\circ$  loading. When this minimum strain is greater than the applied grip strain, amplification arises. Loading cases in which

Loading Direction	axial strain		transverse strains	
	$\epsilon_{\text{grip}} = 10\%$	$\epsilon_{\text{grip}} = 16\%$	$\epsilon_{\text{grip}} = 10\%$	$\epsilon_{\text{grip}} = 16\%$
0°	19%	28%	9%	9%
45°	0%	0%	23%	23%
90°	13%	13%	67%	67%

**Table 3.** Fraction of the neuron volume that experiences a strain that is greater than or equal to the applied strain on surrounding collagen gel for different loading directions.

Loading Direction	Largest 10% of axial strain		Largest 10% of transverse strain	
	$\epsilon_{\text{grip}} = 10\%$	$\epsilon_{\text{grip}} = 16\%$	$\epsilon_{\text{grip}} = 10\%$	$\epsilon_{\text{grip}} = 16\%$
0°	11%*	19%*	4%	6%
45°	6%	10%	17%*	28%*
90°	5%	9%	22%*	37%*

**Table 4.** The minimum strain values experienced by the most-deformed 10% of the neuron. Asterisks indicate strain values that are greater than the applied strain, i.e., applied strain is amplified within neuron.

amplification arises are marked with an asterisk in Table 4.

When the system is loaded at 90°, 10% of the neuron volume experiences a strain amplification of at least a factor of 2 in the transverse direction. When loaded at 45°, the same fraction of the neuron volume experiences an amplification of at least a factor of 1.7. When loaded at 0°, 10% of the neuron volume experiences a strain amplification of at least a factor of 1.1 in the axial direction. The smaller amplification in the axial direction is due to the larger stiffness of the neuron in the axial direction relative to the transverse direction.

In the above analysis, we used the strains along and transverse to the axons, as well as the maximum principal strain as measures of neuron deformation. However, the actual cause of neuronal injury remains unknown. There is still much work to be done in the experimental characterization of neuronal injury and identification of the mechanisms leading to pain.

## 8. Summary

We have presented a general modeling strategy in which (1) a realistic representation of a complex cell geometry is generated from confocal microscopy images of dorsal root ganglion neurons embedded in a collagen gel; (2) the geometric model is converted into a finite-element mesh; (3) a multi-scale model is implemented in the mesh corresponding to the extracellular matrix (collagen gel); and (4) an analysis of the strain distributions within the neuron due to mechanical loading on the extracellular matrix is performed.

The large computational demands that arise from the unstructured mesh of a complex cell geometry coupled with a multi-scale model are accommodated through the AMSI library, which is used to manage the parallel execution spaces of the macroscopic and microscopic scale simulation codes and to plan and enact the parallel communication operations required to couple the two codes together into a multi-scale simulation.

The simulation results for the embedded neuron provides local strain information that is not accessible by current experimental techniques, thereby providing important insights about the mechanism of neuronal injury under mechanical loading. We find

that the strain distribution in the neuron depends strongly on the configuration of the embedded neuron relative to the loading direction, which reflects the anisotropic mechanical properties of the neuron. More importantly, we observe that the applied strain on the surrounding environment is amplified within the neuron for all loading configurations considered. In the most severe cases, the applied strain is amplified by at least a factor of 2 in 10% of the neuron volume.

The work presented in this paper provides an extension to the capability of past modeling strategies by enabling the realistic representation of complex cell geometry into a multi-scale framework. Although several physiologically important mechanisms for the embedded neuron system have been left out, e.g., chemical mediators, calcium signaling, and membrane viability, the results from the simplified system nonetheless provide meaningful results that can be built upon in future work.

## References

- Alastrué V, Rodríguez JF, Calvo B, Doblaré M. 2007. Structural damage models for fibrous biological soft tissues. *International Journal of Solids and Structures.* 44(18-19):5894–5911.
- Ambrosi D, Pezzuto S. 2011. Active Stress vs. Active Strain in Mechanobiology: Constitutive Issues. *Journal of Elasticity.* 107(2):199–212.
- Bonet J, Burton AJ. 1998. A simple orthotropic, transversely isotropic hyperelastic constitutive equation for large strain computations. *Computer Methods in Applied Mechanics and Engineering.* 162(1-4):151–164.
- Bonet J, Wood DR. 2008. *Nonlinear Continuum Mechanics for Finite Element Analysis.* 2nd ed. Cambridge University Press.
- Chandran PL, Barocas VH. 2007. Deterministic Material-Based Averaging Theory Model of Collagen Gel Micromechanics. *Journal of Biomechanical Engineering.* 129(2):137–11.
- Cristini V, Lowengrub J, Nie Q. 2003. Nonlinear simulation of tumor growth. *Journal of Mathematical Biology.* 46(3):191–224.
- Cullen DK, Tang-Schomer MD, Struzyna LA, Patel AR, Johnson VE, Wolf JA, Smith DH. 2012. Microtissue Engineered Constructs with Living Axons for Targeted Nervous System Reconstruction. *Tissue Engineering Part A.* 18(21-22):2280–2289.
- Delalondre F, Smith C, Shephard MS. 2010. Collaborative software infrastructure for adaptive multiple model simulation. *Computer Methods in Applied Mechanics and Engineering.* 199(21-22):1352–1370.
- Dong L, Quindlen JC, Lipschutz DE, Winkelstein BA. 2012. Whiplash-like facet joint loading initiates glutamatergic responses in the DRG and spinal cord associated with behavioral hypersensitivity. *Brain Research.* 1461:51–63.
- Dutov P, Antipova O, Varma S, Orgel JPRO, Schieber JD. 2016. Measurement of Elastic Modulus of Collagen Type I Single Fiber. *Plos One.* 11(1).
- Ehret AE, Itskov M. 2009. Modeling of anisotropic softening phenomena: Application to soft biological tissues. *International Journal of Plasticity.* 25(5):901–919.
- Eppell SJ, Smith BN, Kahn H, Ballarini R. 2006. Nano measurements with micro-devices: mechanical properties of hydrated collagen fibrils. *Journal of The Royal Society Interface.* 3(6):117–121.
- Fletcher DA, Mullins RD. 2010. Cell mechanics and the cytoskeleton. *Nature.*
- Friedl P, Zänker KS, Bröcker EB. 1998. Cell migration strategies in 3-D extracellular matrix: Differences in morphology, cell matrix interactions, and integrin function. *Microscopy Research and Technique.* 43(5):369–378.
- Fung YC. 1993. *Biomechanics.* 2nd ed. Springer-Verlag New York.
- Guido S, Tranquillo RT. 1993. A methodology for the systematic and quantitative study of cell contact guidance in oriented collagen gels. Correlation of fibroblast orientation and gel birefringence. *Journal of Cell Science.* 105(2):317–331.
- Guilak F, Mow VC. 2000. The mechanical environment of the chondrocyte: a biphasic finite element model of cellmatrix interactions in articular cartilage. *Journal of Biomechanics.* 33(12):1663–1673.
- Hashin Z. 1962. The elastic moduli of heterogeneous materials. *Journal of Applied Mechanics.* 29(1):143–150.
- Humphrey JD. 2001. *Cardiovascular solid mechanics: Cells, tissues and organs.* Springer-Verlag New York.
- Humphrey JD, Rajagopal KR. 2002. A constrained mixture model for growth and remodeling of soft tissues. *Mathematical models and methods.* 12(03):407–430.
- Isenberg BC, Williams C, Tranquillo RT. 2006. Small-Diameter Artificial Arteries Engineered In Vitro. *Circulation Research.* 98(1):25–35.
- Ita ME, Zhang S, Holsgrove TP, Kartha S, Winkelstein BA. 2017. The physiological basis of cervical facet-mediated persistent pain: Basic science and clinical challenges. *Journal of Orthopaedic and Sports Physical Therapy.* 47(7):450–461.
- Kallakuri S. 2012. Innervation of cervical ventral facet joint capsule: Histological evidence.

- World Journal of Orthopedics. 3(2):10–5.
- Khalsa PS, Hoffman AH, Grigg P. 1996. Mechanical states encoded by stretch-sensitive neurons in feline joint capsule. *Journal of neurophysiology*. 76(1):175–187.
- Klaas O, Beall MW, Shephard MS. 2013. Construction of models and meshes of heterogeneous material microstructures from image data. *Image-Based Geometric Modeling and Mesh Generation*. 3:171–193.
- Klaas O, Beall MW, Shephard MS. 2014. Generation of geometric models and meshes from segmented data. In: Proc. NAFEMS Americas Conference 2014.
- Lai VK, Hadi MF, Tranquillo RT, Barocas VH. 2013. A Multiscale Approach to Modeling the Passive Mechanical Contribution of Cells in Tissues. *Journal of Biomechanical Engineering*. 135(7):071007.
- Lai VK, Lake SP, Frey CR, Tranquillo RT, Barocas VH. 2012. Mechanical Behavior of Collagen-Fibrin Co-Gels Reflects Transition From Series to Parallel Interactions With Increasing Collagen Content. *Journal of Biomechanical Engineering*. 134(1):011004–19.
- Lake SP, Hadi MF, Lai VK, Barocas VH. 2012. Mechanics of a Fiber Network Within a Non-Fibrillar Matrix: Model and Comparison with Collagen-Agarose Co-gels. *Annals of Biomedical Engineering*. 40(10):2111–2121.
- Lee KE, Thinnis JH, Gokhin DS, Winkelstein BA. 2004. A novel rodent neck pain model of facet-mediated behavioral hypersensitivity: implications for persistent pain and whiplash injury. *Journal of Neuroscience Methods*. 137(2):151–159.
- Limbert G, Middleton J. 2004. A transversely isotropic viscohyperelastic material. *International Journal of Solids and Structures*. 41(15):4237–4260.
- Lindström SB, Kulachenko A, Jawerth LM, Vader DA. 2013. Finite-strain, finite-size mechanics of rigidly cross-linked biopolymer networks. *Soft Matter*. 9(30):7302–12.
- Marquez JP, Elson EL, Genin GM. 2010. Whole cell mechanics of contractile fibroblasts: relations between effective cellular and extracellular matrix moduli. *Philosophical Transactions of the Royal Society A: Mathematical, Physical and Engineering Sciences*. 368(1912):635–654.
- McLain RF, Pickar JG. 1998. Mechanoreceptor endings in human thoracic and lumbar facet joints. *Spine*. 23(2):168–173.
- Menzel A, Kuhl E. 2012. Frontiers in growth and remodeling. *Mechanics Research Communications*. 42:1–14.
- Mofrad MRK, Kamm RD. 2006. Cytoskeletal mechanics. Cambridge University Press.
- Mow VC, Kuei SC, Lai WM, Armstrong CG. 1980. Biphasic creep and stress relaxation of articular cartilage in compression: theory and experiments. *Journal of Biomechanical Engineering*. 102:73–83.
- Peña E, Alastraú V, Laborda A, Martínez MA, Doblaré M. 2010. A constitutive formulation of vascular tissue mechanics including viscoelasticity and softening behaviour. *Journal of Biomechanics*. 43(5):984–989.
- Peter SJ, Mofrad MRK. 2012. Computational Modeling of Axonal Microtubule Bundles under Tension. *Biophysical Journal*. 102(4):749–757.
- Pizzo AM. 2005. Extracellular matrix (ECM) microstructural composition regulates local cell-ECM biomechanics and fundamental fibroblast behavior: a multidimensional perspective. *Journal of Applied Physiology*. 98(5):1909–1921.
- Quindlen JC, Stolarski HK, Johnson MD, Barocas VH. 2016. A multiphysics model of the Pacinian corpuscle. *Integrative Biology*. 8:1111–1125.
- Quinn KP, Winkelstein BA. 2008. Altered collagen fiber kinematics define the onset of localized ligament damage during loading. *Journal of Applied Physiology*. 105(6):1881–1888.
- Quinn KP, Winkelstein BA. 2009. Vector correlation technique for pixel-wise detection of collagen fiber realignment during injurious tensile loading. *Journal of Biomedical Optics*. 14(5):054010–10.
- Schneider CA, Rasband WS, Eliceiri KW. 2012. NIH Image to ImageJ: 25 years of image analysis. *Nature Methods*. 9(7):671–675.
- Schultz RA, Miller DC, Kerr CS, Micheli L. 1984. Mechanoreceptors in human cruciate liga-

- ments. a histological study. Journal of Bone and Joint Surgery - American Volume.
- Shephard MS. 2000. Meshing environment for geometry-based analysis. International Journal for Numerical Methods in Engineering. 47:169–190.
- Simmetrix. 2017. <http://www.simmetrix.com>.
- Simon BR. 1992. Multiphase poroelastic finite element models for soft tissue structures. Applied Mechanics Reviews. 45(6):191–218.
- Simon M, Dokukin M, Kalaparthi V, Spedden E, Sokolov I, Staii C. 2016. Load Rate and Temperature Dependent Mechanical Properties of the Cortical Neuron and Its Pericellular Layer Measured by Atomic Force Microscopy. Langmuir. 32(4):1111–1119.
- Sperry MM, Ita ME, Kartha S, Zhang S, Yu YH, Winkelstein B. 2017. The Interface of Mechanics and Nociception in Joint Pathophysiology: Insights From the Facet and Temporomandibular Joints. Journal of Biomechanical Engineering. 139(2):021003–13.
- Stylianopoulos T, Barocas VH. 2007. Volume-averaging theory for the study of the mechanics of collagen networks. Computer Methods in Applied Mechanics and Engineering. 196(31–32):2981–2990.
- Svensson RB, Hassenkam T, Hansen P, Magnusson SP. 2010. Viscoelastic behavior of discrete human collagen fibrils. Journal of the Mechanical Behavior of Biomedical Materials. 3(1):112–115.
- Syedain ZH, Graham ML, Dunn TB, O'Brien T, Johnson SL, Schumacher RJ, Tranquillo RT. 2017. A completely biological “off-the-shelf” arteriovenous graft that recellularizes in baboons. Science Translational Medicine. 9(414):eaan4209.
- Tobin WR, Chan VWL, Picu CR, Barocas VH, Shephard MS. in preparation. The adaptive multiscale simulation infrastructure - methods and soft tissue example simulation. .
- Tower TT, Neidert MR, Tranquillo RT. 2002. Fiber alignment imaging during mechanical testing of soft tissues. Annals of Biomedical Engineering. 30(10):1221–1233.
- Whitaker S. 1999. The method of volume averaging. Springer.
- Zhang S, Cao X, Stablow AM, Shenoy VB, Winkelstein BA. 2016. Tissue Strain Reorganizes Collagen With a Switchlike Response That Regulates Neuronal Extracellular Signal-Regulated Kinase Phosphorylation In Vitro: Implications for Ligamentous Injury and Mechanotransduction. Journal of Biomechanical Engineering. 138(2):021013–12.
- Zhang S, Singh S, Winkelstein BA. 2017a. Collagen organization regulates stretch-initiated pain-related neuronal signals in vitro: Implications for structure-function relationships in innervated ligaments. Journal of Orthopaedic Research. 3:10–8.
- Zhang S, Zhao E, Winkelstein BA. 2017b. A Nociceptive Role for Integrin Signaling in Pain After Mechanical Injury to the Spinal Facet Capsular Ligament. Annals of Biomedical Engineering:1–13.

## Appendix A: Derivation of $P_2$ from $\alpha$ and $\delta$ of the QPLI method

Consider a distribution of orientation  $\theta$  for pixel  $i$  as

$$p_i(\theta) = q_i + r_i \cos^2(\theta - \alpha_i) \quad \text{for } \theta \in (0, \pi), \quad (1)$$

where  $\alpha_i$  is the alignment measured at pixel  $i$  by the QPLI method and  $q_i$  and  $r_i$  are constants for the  $i^{th}$  pixel. Applying the normalization

$$\int_0^\pi p_i(\theta) d\theta = 1, \quad (2)$$

a relationship between  $q_i$  and  $r_i$  is obtained:

$$\pi q_i + \frac{\pi}{2} r_i = 1. \quad (3)$$

Using the relationship in Eq. (3), Eq. (1) can be rewritten as

$$p_i(\theta) = q_i + \frac{2}{\pi}(1 - \pi q_i) \cos^2(\theta - \alpha_i) \quad (4)$$

The orientation tensor for each pixel can be written in terms of  $p_i(\theta)$  as

$$\mathbf{A}^i = \begin{bmatrix} \int_0^\pi p_i(\theta) \cos^2(\theta) d\theta & \int_0^\pi p_i(\theta) \sin(\theta) \cos(\theta) d\theta \\ \int_0^\pi p_i(\theta) \sin(\theta) \cos(\theta) d\theta & \int_0^\pi p_i(\theta) \sin^2(\theta) d\theta \end{bmatrix} = \frac{1 - \pi q_i}{4} \begin{bmatrix} \cos(2\alpha_i) & \sin(2\alpha_i) \\ \sin(2\alpha_i) & -\cos(2\alpha_i) \end{bmatrix}, \quad (5)$$

where the eigenvalues of  $\mathbf{A}^i$  are

$$\Lambda_1 = \frac{1 + \pi q_i}{4} \quad \text{and} \quad \Lambda_2 = \frac{3 - \pi q_i}{4}. \quad (6)$$

The retardation at each pixel,  $\delta_i$ , is related to the eigenvalues through a proportionality constant,  $C$ , by

$$\delta_i = C|\Lambda_2 - \Lambda_1| = C \left( \frac{1 - \pi q_i}{2} \right). \quad (7)$$

From Eq. (7), the constant  $q_i$  can be written in terms of the retardation as

$$q_i = \frac{1}{\pi} \left( 1 - \frac{2\delta_i}{C} \right), \quad (8)$$

and the distribution at pixel  $i$  from Eq. (4) can be rewritten as

$$p_i(\theta) = \frac{C - 2\delta_i}{\pi C} + \frac{4\delta_i}{\pi C} \cos^2(\theta - \alpha_i). \quad (9)$$

The distribution of orientation  $\theta$  for the entire image is simply the average over the distribution of each pixel

$$p(\theta) = \frac{1}{N} \sum_{i=1}^N p_i(\theta) = \frac{1}{N} \sum_{i=1}^N \left[ \frac{C - 2\delta_i}{\pi C} + \frac{4\delta_i}{\pi C} \cos^2(\theta - \alpha_i) \right], \quad (10)$$

which is the equation presented in Eq. (10).

## Appendix B: Varying Axial Stiffness ( $t$ ) in the Cell Body

The complementary cumulative distribution function for different axial stiffnesses of the cell body (different values of  $t$ ) are plotted in Fig. 1 for the  $0^\circ$  loading case for a grip strain of 16% on the collagen gel. These results suggest that the strain distribution within the neurons is insensitive to the axial distribution of stiffness of the cell body.

The negative values of strain seen in the distributions are due to lateral contraction that arises from the Poisson effect.

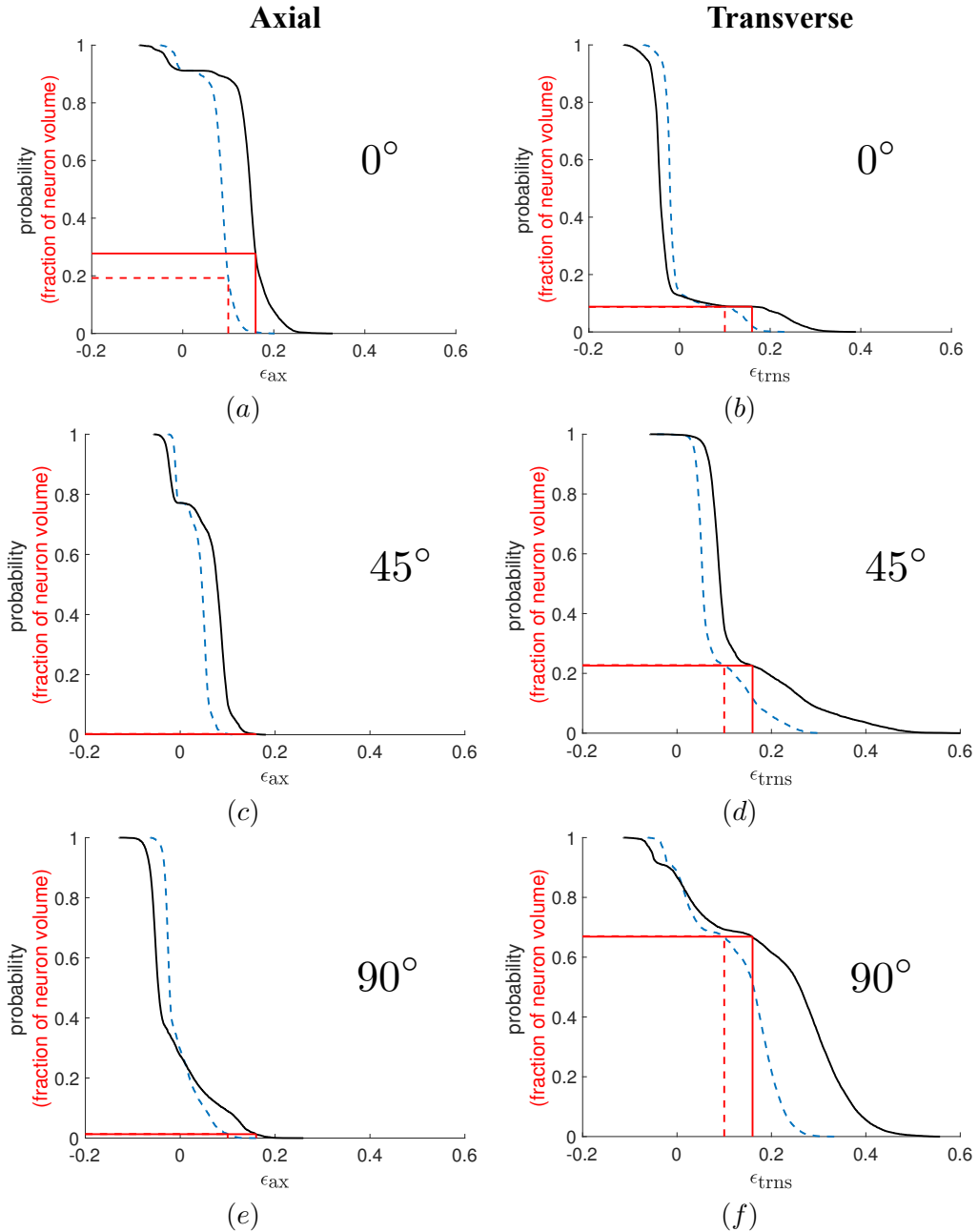


**Figure 9.** Complementary cumulative distribution functions for axial (left column) and transverse (right column) strains in neuron for  $0^\circ$  (top row),  $45^\circ$  (middle row), and  $90^\circ$  (bottom row) loading. Distributions for 10% (blue dashed line) and 16% (black solid line) grip strains are plotted for all loading directions. The dashed and solid red lines indicate the approximate fraction of the neuron volume that experience a strain of greater than or equal to 10% and 16%, respectively.

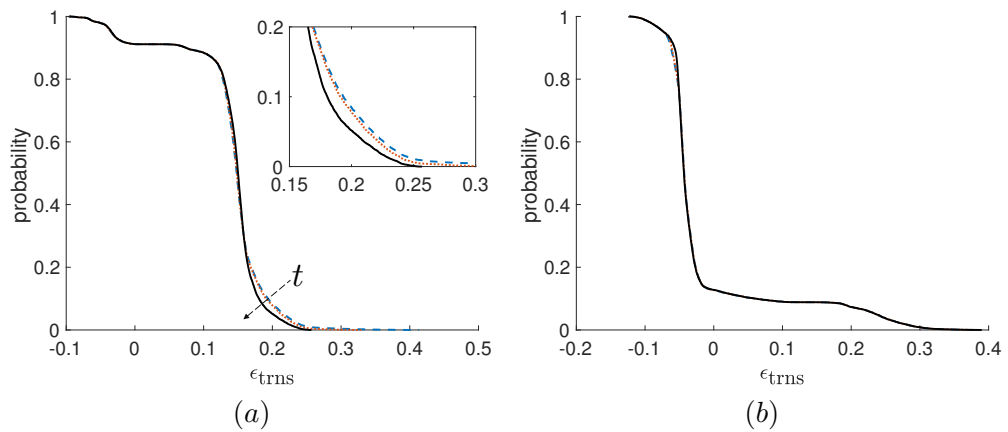


**Figure 1.** Complimentary cumulative distribution functions for (a) axial and (b) transverse strains in the neuron due to a  $0^\circ$  load of 16% grip strain. The distributions are for axial cell-body stiffnesses corresponding to  $t=28 \mu\text{m}$  (blue dashed line),  $30 \mu\text{m}$  (red dotted line), and  $50 \mu\text{m}$  (black solid line). The dashed arrow in (a) indicates the direction of increasing  $t$  and the inset in (a) enlarges the heel of the distribution to aid visual interpretation.